Eur. Phys. J. D **10**, 123–129 (2000)

THE EUROPEAN PHYSICAL JOURNAL D

EDP Sciences

Cu–Ni alloy nanocluster formation by ion implantation in silicate glasses: Structure and optical properties

F. D'Acapito[1], G. Battaglin[2], E. Cattaruzza[2,a], F. Gonella[2], C. Maurizio[3], P. Mazzoldi[3], S. Mobilio[4], and F. Zontone[5]

[1] INFM, European Synchrotron Radiation Facility, GILDA-CRG, B.P. 220, 38043 Grenoble, France
[2] INFM, Dipartimento di Chimica Fisica, Università di Venezia, Dorsoduro 2137, 30123 Venezia, Italy
[3] INFM, Dipartimento di Fisica, Università di Padova, via Marzolo 8, 35131 Padova, Italy
[4] Università Roma III, via della Vasca Navale 84, 00146 Roma, Italy
[5] European Synchrotron Radiation Facility, B.P. 220, 38043 Grenoble, France

Received 6 May 1999 and Received in final form 22 September 1999

Abstract. Sequential ion implantation (copper and nickel) in silica and soda-lime glasses has been performed. The formation of copper-nickel alloy nanocluster in the glass host has been evidenced by synchrotron radiation-based techniques, namely X-ray diffraction and absorption spectroscopy. The nanocrystals' lattice parameter value was estimated, indicating the formation of $Cu_{55}Ni_{45}$ alloy particles. Optical absorption spectra are also discussed.

PACS. 61.46.+w Clusters, nanoparticles, and nanocrystalline materials – 61.10.-i X-ray diffraction and scattering – 61.10.Ht X-ray absorption spectroscopy: EXAFS, NEXAFS, XANES, etc.

1 Introduction

Glasses containing nanometer-sized metal clusters exhibit intensity-dependent refractive index values several orders of magnitude larger than that of silica glass, owing to dielectric and quantum confinement effects [1]. Transition metals are particularly interesting since they also exhibit peculiar magnetic properties [2]. Ion implantation has been exploited as one of the most effective techniques for creating metal nanoclusters in glasses [2–11]. The preparation of "mixed" colloidal structures, containing clusters of either different metals or metallic alloys, has also recently attracted attention, due to the possibility of tailoring the performances of these composites. For example, the optical linear absorption was studied [12] after sequential implantation of gold and copper in glass, obtaining results that suggest the formation of alloy clusters. In spite of the non-equilibrium characteristics of the ion implantation process, the important role of chemical driving forces has been recognised in determining the final configuration of ion-implanted materials [13–17], even more so when the process involves different sequentially implanted species [18–23]. Reasonably, both the ion implantation as a synthesis method and the nanometric dimension of the formed metallic particles can influence in a very complex way the alloy formation steps: in particular, the relative importance of the thermodynamic mechanism and the kinetic one is far from completely understood.

Sequential copper + nickel implanted glass is particularly interesting because the two metals exhibit complete miscibility for all compositions in the bulk phase, forming an *fcc* alloy whose lattice parameter a_0 follows with good approximation the Vegard law [24]. The free energy variation, ΔG, involved in the Cu–Ni alloy formation has a minimum (-2.8 kJ mol^{-1}) at 973 K for $\approx 40\%$ Ni composition [25]. For copper + nickel implanted silica, transmission electron microscopy (TEM) measurements indicate the presence of spherical metallic clusters, with diameter up to 10 nm, increasing with the local metal concentration [9]. A recent morphological study on the copper + nickel implanted glass system [26], based on TEM and grazing incidence small angle X-ray scattering (GISAXS), has shown the formation of roughly spherical metallic particles. Strobel *et al.* [27] used a kinetic 3D lattice Monte-Carlo model to study the diffusion, precipitation and interaction kinetics of sequentially implanted elements in a chemically neutral matrix. For the Cu–Ni pair, their approach indicates that the formation of both single-element nanoclusters and core-shell structures are disfavoured, yet not indicating an ordered compound phase formation. In this case, the model only suggests that cluster formation and composition will be determined mainly by the kinetics. Actually, the local temperature during the second ion irradiation can alter the level of collisional mixing between the two metallic species by thermodynamically-driven atomic movements: the nonlocal and nonequilibrium nature of the heat transfer processes around nanoparticles [28] can induce very high

[a] e-mail: cattaruz@unive.it

Table 1. Implantation parameters (fluence and energy) of the investigated samples.

sample name	substrate	1st irradiation		2nd irradiation	
Ni(s)	silica	6×10^{16} Ni^+cm^{-2}	90 keV		
Ni(g)	soda-lime glass	6×10^{16} Ni^+cm^{-2}	90 keV		
CuNi(s)	silica	6×10^{16} Cu^+cm^{-2}	90 keV	6×10^{16} Ni^+cm^{-2}	100 keV
CuNi(g)	soda-lime glass	6×10^{16} Cu^+cm^{-2}	90 keV	6×10^{16} Ni^+cm^{-2}	100 keV
Cu(s)	silica	6×10^{16} Cu^+cm^{-2}	160 keV		
Cu(g)	soda-lime glass (0.1 mm thick)	6×10^{16} Cu^+cm^{-2}	160 keV		
HF-Cu(s)	silica	1×10^{17} Cu^+cm^{-2}	160 keV		
HF-Cu(g)	soda-lime glass	1×10^{17} Cu^+cm^{-2}	160 keV		

particle temperature. Therefore, the problem of predicting the final configuration of a double Cu + Ni ion implantation on silicate glasses becomes quite complex.

In this work we have performed synchrotron radiation-based (X-ray diffraction and absorption spectroscopy) characterization to directly investigate the structure of the metallic particles in Cu+Ni implanted silicate glasses. Optical absorption spectra were also discussed.

2 Experimental procedure

Silica (type II Heraeus Herasil, hereafter called "s" substrate) and commercial soda-lime glass ("g" substrate) slides 1 mm thick (except for Cu(g) sample, 0.1 mm thick) were implanted sequentially with Cu and Ni ions. The preparation details (implant fluence and energy) are summarized in Table 1. The substrates were implanted at room temperature (*RT*) without subsequent annealing. Simulations of the implant profiles were performed with the TRIM code [29], yielding a projected range of 70 nm (Cu) and 80 nm (Ni). The choice of a different projected range comes from the experimental evidence of a deeper penetration of implanted copper atoms inside both silica and soda-lime glass, if compared to the TRIM prediction [8]. The use of low energies (keV range) allows the attainment of high local metal concentration, leading to cluster formation.

Samples were characterized by optical absorption spectroscopy in the 1.5–3.5 eV energy range (820–350 nm of wavelength) using a Varian CARY 5E UV-VIS-NIR dual-beam spectrophotometer.

Extended X-ray absorption fine structure (EXAFS) measurements were performed at the European Synchrotron Radiation Facility (ESRF) on the Italian beamline GILDA, with a bending magnet device source. All spectra were recorded at liquid nitrogen temperature (LNT), to reduce atomic thermal vibration. The sagittally focusing monochromator, used in the so-called dynamical focusing mode [30], was equipped with two Si(311) crystals. Harmonic rejection was achieved by two Pd coated mirrors working at 3 mrad with an energy cut-off of 23 keV. The flux on the samples was of the order of 2×10^{10} photons s^{-1}. Measurements were performed at both Cu and Ni K-edges in fluorescence mode. The signal collection was achieved by a high-purity 7-elements Ge detector, keeping the total count rate per single element below 2×10^4 cps, to assure a linear response. The use of this kind of detector allows to exclude both the Ni fluorescence contributions in the case of the Cu K-edge measurements and that of the elastic scattering.

Due to the peculiar nature of the samples, X-ray diffraction measurements were performed in grazing incidence configuration to enhance the cluster signal contribution (grazing incidence X-ray diffraction, GIXRD). Details on this unusual experimental technique are reported elsewhere [31]. Measurements were performed at ESRF on the ID9 beamline, at *RT*. The X-ray beam coming from an undulator source was monochromatised by a Laue monochromator sagittally focused in the horizontal plane. A beam of 10 (hor) × 20 (vert) μm^2 section was available at 0.4555 Å with a flux of about 5×10^{10} photons s^{-1}. X-ray reflectivity curves from the double-implanted samples (CuNi(s), CuNi(g)) were measured to fix the optimal incidence angle. The angle, chosen at the first bump in the falling edge of the reflectivity curve, is around 0.08°: this corresponds to a beam footprint of 7 mm on the sample. Data were collected with an image plate (IP) detector placed at 342.6 mm from the sample. IP exposure times were in the few minutes range. An aluminum filter 0.5 mm thick was placed in front of the IP to stop the fluorescence signals (Cu, Ni and soda-lime glass impurities) from the sample. The usual scattering curves were obtained by azimuthal integration of the images in a $\sim 170°$ wide angular sector; the image treatment was performed with the Fit2D program [32]. The incident wavelength and the exact sample-to-plate distance were determined by means of a reference standard (Si crystalline powder diffraction pattern).

3 Results

3.1 Optical absorption spectroscopy

The optical absorption spectra of the samples are shown in Figure 1 (top: silica substrate and bottom: soda-lime glass substrate). In the framework of Maxwell-Garnett effective medium theory [33], the absorption coefficient for a composite consisting of small particles of complex dielectric constant $\varepsilon_m(\omega) = \varepsilon_1(\omega) + i\varepsilon_2(\omega)$ occupying a relative

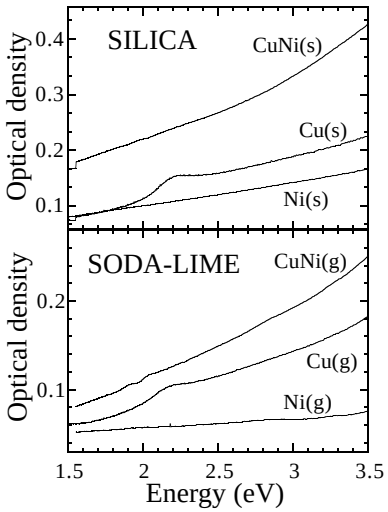

Fig. 1. Absorption spectra of the single- and double-implanted glasses; silica substrate (top); soda-lime substrate (bottom).

volume fraction $p \ll 1$ is

$$\alpha = 9p\frac{\omega\varepsilon_{\rm h}^{3/2}}{c}\frac{\varepsilon_2}{(\varepsilon_1+2\varepsilon_{\rm h})^2+\varepsilon_2^2}$$

where $\varepsilon_{\rm h}$ is the surrounding medium dielectric constant and c is the velocity of light. Surface plasmon resonance (SPR) may appear as characteristic band(s) in the optical absorption spectra [34], depending on the values of the dielectric functions of both metal and glass host. For copper nanoclusters embedded in silica or soda-lime glasses, the SPR is centered at about 2.2 eV of photon energy ([11] and references therein). On the other hand, nickel clusters embedded in the same substrates do not originate any SPR in the visible region [34].

The Cu(s) sample, *i.e.*, silica irradiated with copper ions, exhibits an SPR absorption band (Fig. 1, top) indicating the presence of metallic clusters in the nanometer size range. A similar behaviour is observed in the Cu(g) sample (soda-lime substrate), even if only a faint SPR originates (Fig. 1, bottom), indicating the formation of a lower number of copper nanoclusters. It is worth stressing here that Cu^+ or Cu^{2+} ions do not exhibit absorption band structure in this energy region. Thus, the observation of the SPR is a reliable check for the presence of metallic copper particles, even in the presence of a dominating copper oxide phase. Finally, regardless of the substrate, the sequentially implanted samples do not exhibit any absorption band.

3.2 EXAFS spectroscopy

X-ray absorption spectroscopy was performed to investigate the local order around the implanted atoms. Data analysis was performed by Fourier filtering and multiparameter fit on the filtered data [35]. Experimental backscattering amplitudes and phases were extracted from low temperature (LNT) spectra of model compounds:

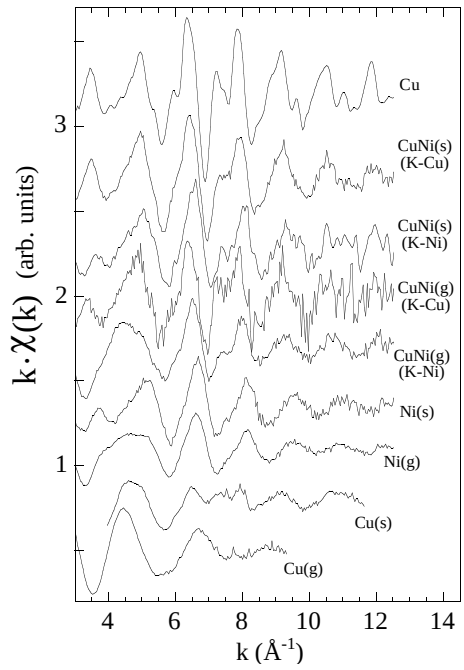

Fig. 2. $k\chi(k)$ EXAFS curves of single and double-implanted samples compared to EXAFS signal of Cu metal foil (in different scale).

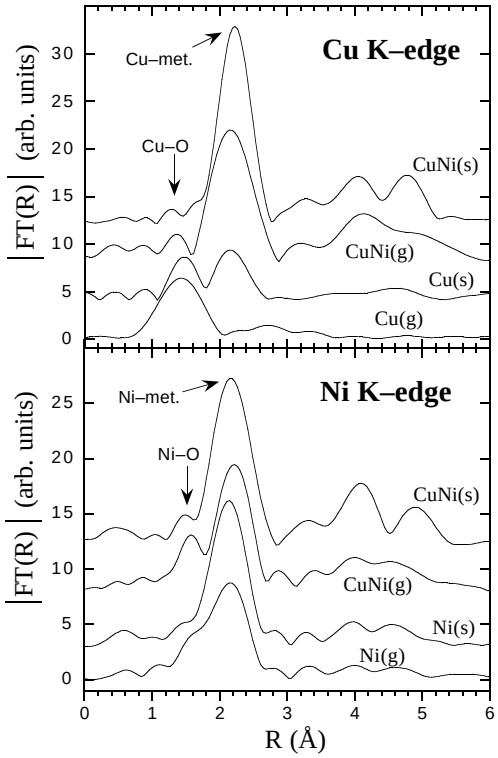

Fig. 3. Moduli of the Fourier transforms of k^3 weighted spectra for k in the [3–13] Å^{-1} window.

metallic Cu and Ni foils for the metal-metal pairs and Cu_2O and NiO powders for the metal-oxygen couples. The backscattering parameters being nearly identical for Cu and Ni, the metal-metal shells were fitted with the

Table 2. Results of the EXAFS analysis. N and R parameters are the coordination number and the first shell distance, respectively. $\Delta\sigma^2$ values are relative to the model compounds. Parameters without error bars were kept fixed during the fit.

sample, edge	N (atoms)	R (Å)	$\Delta\sigma^2$ (10^{-4} Å^2)
Cu foil[a]	12 Cu	2.5561	
Ni foil[a]	12 Ni	2.4918	
Cu_2O[a]	2 O	1.849	
CuO[b]	2 O	1.951	
	2 O	1.961	
NiO[a]	6 O	2.0842	
HF-Cu(s)	7 ± 1 Cu	2.55 ± 0.01	0 ± 5
HF-Cu(g)	2.8 ± 0.5 Cu	2.56 ± 0.03	2 ± 15
	3 ± 2 O	1.89 ± 0.02	60 ± 30
Cu(s)	1.4 ± 0.3 Cu	2.52 ± 0.02	12 ± 5
	1 ± 2 O	1.87 ± 0.04	0 ± 4
Cu(g)	4 O	1.87 ± 0.02	45 ± 7
Ni(s)	5 ± 2 Ni	2.46 ± 0.03	32 ± 36
	1.0 ± 0.5 O	1.99 ± 0.02	119 ± 48
Ni(g)	4 ± 1 Ni	2.47 ± 0.02	48 ± 20
	5 ± 2 O	2.00 ± 0.03	100 ± 45
CuNi(s) K-Cu	7 ± 1 Met	2.53 ± 0.02	32 ± 18
CuNi(g) K-Cu	4.2 ± 0.6 Met	2.52 ± 0.02	-13 ± 36
	0.8 ± 0.5 O	1.82 ± 0.05	-20 ± 56
CuNi(s) K-Ni	5 ± 1 Met	2.51 ± 0.02	15 ± 32
	4 ± 1 O	1.99 ± 0.05	119 ± 96
CuNi(g) K-Ni	3 ± 1 Met	2.52 ± 0.02	0 ± 28
	4 ± 1 O	1.95 ± 0.02	75 ± 40

[a] From reference [36]. [b] From reference [51].

phase and amplitude relative to the absorbing atom (Cu–Cu and Ni–Ni phases for Cu-metal and Ni-metal pairs, respectively). In the quantitative study, error bars were calculated through a statistical χ^2 analysis considering a 95% confidence level. The $k\chi(k)$ curves (k = photoelectron wavenumber, $\chi(k)$ = absorption coefficient interference function) obtained from absorption spectra and the relative Fourier transforms (FT) are shown in Figures 2 and 3, respectively. In Figure 3, peaks located at about 2.2 Å correspond to the metal-metal correlation, while the signals centered at about 1.5 Å are due to metal-oxygen coordination. We explain this by assuming the coexistence of a metallic cluster phase and an oxidized phase, consisting of copper (nickel) ions at the cluster/glass interface and/or dispersed in the glass matrix.

Structures in the FT above 3 Å are particularly evident in the sequentially implanted samples and are related to the higher coordination shells of the *fcc* structure, indicating the presence of relatively large particles. Structural data obtained from the quantitative analysis are collected in Table 2. In the case of well distinct metal-metal and metal-oxygen coordination peaks (see Fig. 3), data were processed by filtering separately the two peaks. For the other cases, filtered data were fitted to a two-shell model except for the Cu(g) sample, for which a meaningful data analysis was possible by assuming the presence of the oxidized copper species only.

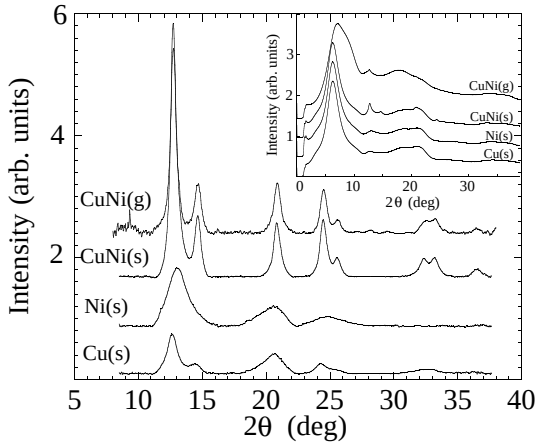

Fig. 4. GIXRD radial integrated spectra after silica background subtraction. In the inset the raw data are shown (normalized to 1 on the first scattering maximum).

The most interesting result comes from the metal-metal nearest-neighbour distance detected in the double-implanted samples. Within the experimental errors, from both the Cu and Ni K-edge spectra we calculated the same distance value of 2.52 Å. This occurred for both the CuNi(s) and the CuNi(g) samples. The measured metal-metal nearest-neighbour distance corresponds in the *fcc* phase to a lattice parameter $a_0 = 3.56$ Å: this value lies between those of the two bulk metal phases [36] (see Tab. 2).

In almost all samples the presence of an oxide phase is revealed. The coexistence of oxide and metal phases makes difficult the determination of the valence state from considerations of the absorption edge position. From previous investigations on Cu-implanted silica [22,37] and soda-lime glasses [38], and on Cu^+–Na^+ exchanged soda-lime glasses [39,40], it is well established that the preferred valence state of copper in these substrates is Cu^+, with the detectable presence of Cu^{2+} only at low metal concentrations. The Cu^0 valence state dominates only for high local copper concentration (larger than, say, about 5% atomic fraction). In the Cu(g) sample the copper oxide phase dominates, characterized by a coordination distance $R^{\text{Cu–O}} = 1.87 \pm 0.02$ Å, the same observed in the Cu(s) sample. For both Ni(s) and Ni(g) samples, EXAFS analyses gave the same Ni–O first shell distance ($R^{\text{Ni–O}} = 2.00 \pm 0.02$ Å). It is worth noting that this spacing is lower than that observed in NiO_6 octahedral clusters in aqueous solutions ($R^{\text{Ni–O}} = 2.06$ Å) [41]. For the CuNi(s) and CuNi(g) samples, the Ni–O first shell distance is very similar to that found in the Ni-implanted samples.

3.3 GIXRD analysis

Samples were also investigated by grazing incidence X-ray diffraction, to obtain a more precise determination of the lattice parameter and an estimate of the particle diameters. For all the samples, the intensity of the diffraction rings in the IP images was uniform along the azimuthal

Table 3. Lattice parameters a_0 (with the corresponding nearest-neighbour distances R_{NN}) and particle diameters D from the GIXRD analysis. Error bars are calculated at a 95% confidence level. R_{NN} values are in good agreement with those from EXAFS. Pure elements bulk values are also shown for comparison (Ref. [36]).

sample	a_0 (Å)	R_{NN} (Å)	D (Å)
CuNi(s)	3.565 ± 0.010	2.521 ± 0.007	70 ± 10
CuNi(g)	3.559 ± 0.012	2.517 ± 0.008	50 ± 10
Ni(s)	3.490 ± 0.020	2.468 ± 0.014	20 ± 10
HF-Cu(s)	3.597 ± 0.005	2.543 ± 0.004	100 ± 10
Cu(s)	3.590 ± 0.010	2.539 ± 0.007	25 ± 10
Ni bulk	3.524	2.492	–
Cu bulk	3.615	2.556	–

angle, indicating the absence of preferential orientation of the crystallites. Data analysis was performed following a procedure described in detail elsewhere [42]. After the angular integration on the image, the spectrum of the unimplanted glass was subtracted from the treated one in order to extract the pure cluster signal. The comparison between the raw and subtracted data is shown in Figure 4. Only Cu(s), Ni(s) CuNi(s) and CuNi(g) samples exhibit diffraction peaks and these are in the typical positions of the *fcc* lattice. The determination of the lattice parameters was performed both by direct peak position analysis and Rietveld refinement [43], finding identical values. The peak profile was fitted with a pseudo-Voigt function, fixing the calculated Gaussian contribution due to instrumental broadening. The results of the investigation are reported in Table 3: again, the lattice parameters a_0 in CuNi(s) and CuNi(g) are in between the bulk copper and nickel values, in agreement with the EXAFS findings. The peak width analysis reveals bigger particles in sequentially implanted samples than in single implanted ones.

3.4 Discussion

EXAFS data taken at both copper and nickel K-edges, and GIXRD measurements give a remarkable agreement in the determination of the nanoparticles' lattice parameters a_0. In particular, the a_0 value of the nanoclusters in sequentially implanted samples is always halfway between the pure copper and nickel bulk values. Structural determinations indicate the formation of Cu_x–$Ni_{(100-x)}$ alloy nanoclusters, with $x = 59 \pm 11$ for CuNi(s) and $x = 53 \pm 14$ for CuNi(g) samples (from GIXRD determination of a_0 and Ref. [24]). We also considered different possible origins for the detected a_0 values. In the case of single copper implantations (Tab. 2), the contraction of the lattice parameter can be ascribed to the limited size of clusters, as already observed in the literature [44,45], due to the matrix hydrostatic pressure (droplet model). This is indeed the case for Cu(s) and Ni(s) samples, where the particles are sufficiently small to justify the observation of the contraction of the lattice parameter, in agreement with molecular dynamics simulations for 309 atoms ($D \approx 25$ Å) cubo-octahedral clusters [46] ($a_0^{\mathrm{Ni}} = 3.500$ Å, $a_0^{\mathrm{Cu}} = 3.568$ Å). However, a larger contraction is observed for 70 Å and 50 Å diameter clusters in double implanted samples than for the 25 Å diameter clusters in the single implanted Cu(s) (Tab. 3). Moreover, if we suppose the clusters are of nickel, in the CuNi(s) and CuNi(g) samples an expansion of the lattice parameter is observed. All these observations are not explainable with the droplet model. Finally, the high fluence (HF) copper implanted samples exhibit larger lattice parameters, related to bigger clusters. From all these considerations, the most realistic picture is to consider the formation of copper-nickel alloy nanoclusters in the sequentially implanted samples, with the a_0 changing due to the Vegard behaviour of the system.

Knowing the cluster structure, we have then calculated the expected optical absorption response and compared it with the experimental spectra reported in Figure 1. To calculate the optical absorption of a composite material, one must know the bulk dielectric function ε of the clusters as well as its size dependence. For copper-nickel alloy clusters, the real and imaginary parts of ε ($\varepsilon_1^{\mathrm{bulk}}$, $\varepsilon_2^{\mathrm{bulk}}$) and E_{p} (the plasma energy) can be evaluated, in a first approximation, by a linear interpolation between the pure metal values weighted by the respective atomic fraction. We calculated these functions for 0 to 100% Ni content by taking the values of ε from references [47–49]. The size dependence of ε for metal nanoclusters of radius R can be calculated following either classical or quantum mechanical [34,50] treatments. Dealing with relatively large particles, we considered the classical formula

$$\varepsilon_2(R,E) = \varepsilon_2^{\mathrm{bulk}} + \frac{h}{2\pi}\frac{\nu_{\mathrm{F}}}{R}\frac{E_{\mathrm{p}}^2}{E^3}$$

where h and ν_{F} are the Planck constant and the Fermi velocity, respectively. The Fermi velocity is re-scaled calculating the alloy electron density in terms of conduction electrons per atom and of the Vegard approximation of the alloy lattice parameter. The calculated optical absorption spectra for 70 Å diameter alloy clusters of different nickel content and embedded in silica are shown in Figure 5. For soda-lime glass, spectra are quite similar. The simulation, even in this rough approximation, clearly shows that in both silica and soda-lime glass the SPR is expected to disappear for copper-nickel alloy nanoclusters with growing nickel content. No SPR is expected for pure nickel nanoclusters, as observed in the Ni(s) and Ni(g) samples. Copper-nickel alloy clusters form in the glass upon sequential double ion implantation, and their optical response is in agreement with theoretical calculations.

The EXAFS investigation has also evidenced the presence of oxidized ions not revealed by diffraction, indicating that the oxides are amorphous. From the previous considerations, the main copper oxidation state should be +1, as confirmed by the bond lengths with O, nearer to that for Cu^+ oxide (1.8490 Å) [36] than to Cu^{2+} oxide (1.95−1.96 Å) [51]. The presence of the oxidized phase is responsible for the lowering of the apparent metal-metal coordination numbers N^{mm} for all samples: while all the

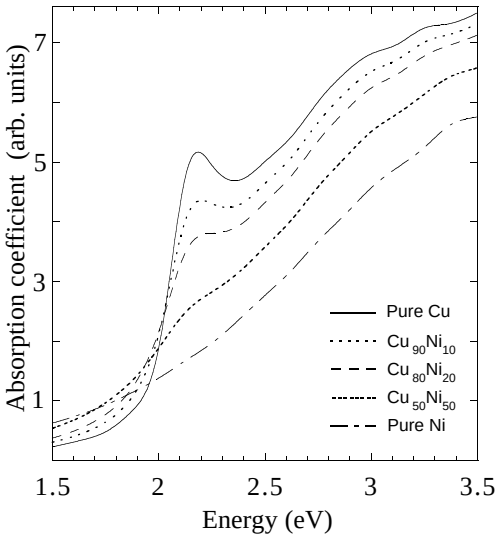

Fig. 5. Simulated optical absorption coefficient for copper-nickel alloy nanoclusters ($D = 70$ Å) embedded in silica glass, as a function of the alloy composition.

absorbing atoms contribute to the edge jump for the normalization of the EXAFS oscillations, only a part of them contribute to the (say) high frequency oscillations of the metal-metal coordination. In this way, the value of the apparent metal-metal coordination number N^{mm} is given by

$$N^{mm} = N_0^{mm} x$$

where x is the fraction of atoms in the metallic phase, and N_0^{mm} is the expected value of N^{mm} (*i.e.*, with no oxide phases) taking into account the size effects. In fact, the limited cluster size tends to reduce N^{mm}: expected values can be calculated by the formula in reference [52]. However, for a copper or nickel *fcc* cluster with $D = 25$ Å, the expected N_0^{mm} value is 10, significantly larger than the observed ones. Thus, the importance of the oxide phase is evidenced. In general, implanted silica samples exhibit higher N^{mm} as well as clusters of bigger dimension than soda-lime glass samples, for the same implant conditions.

An empirical expression for the equilibrium redox ratio of the general reaction $4\mathrm{M}^{n+} + 2n\mathrm{O}^{2-} \rightleftarrows 4\mathrm{M} + n\mathrm{O}_2$ in glass melt (at 1400 °C in air) was obtained as a function of the "optical basicity", Λ, of the glass [53]. M is a generic metallic element. The expressions found indicate that for copper (under the described equilibrium conditions) the +1 oxidation state is the favoured one; the more the melt basicity Λ, the more favourite is the Cu^+, for example passing from silica ($\Lambda = 0.48$) to a typical soda-lime glass ($\Lambda \approx 0.6$). For nickel, the +2 oxidation state is the favoured one, even if the trend is opposite to that of copper. Obviously, we are well aware that these kind of considerations cannot be directly applied to an out-of-equilibrium process as the ion implantation is: however, they can give interesting suggestions to the understanding of the compound formation in ion-implanted glasses. Actually, if exposed to ion implantation, soda-lime glasses exhibit a higher chemical reactivity than silica. This is also due to the high content of non-bridging oxygens in soda-lime glass. Previous investigations on Cu-implanted soda-lime glass by means of depth profiling X-ray photoelectron and X-ray-excited Auger electron spectroscopies [22] showed a marked depletion of both Na^+ and Ca^{2+} ions in the implanted region: the ion irradiation leaves many free reactive sites for the incoming (copper) ions.

Cu(g) sample does not exhibit any trace of metal in EXAFS (and GIXRD), whereas a faint absorption is observed in the optical spectra. This is not a contradiction but a consequence of the different sensitivities of the techniques to the phases involved. While copper oxides do not contribute at all to the optical absorption in the region considered, the EXAFS signal is the sum of the signals coming from the single phases weighted by the corresponding atomic fraction. Similarly, the GIXRD signal due to the crystalline phases is superimposed to a dominating glass scattering signal (see inset in Fig. 4). In the case of a situation with, namely, only few % of metal (in sufficiently sized clusters, *i.e.*, $D > 30$ Å) and the remaining in the oxide phase, no metal-metal coordination will be detected neither by EXAFS (being dominated by the low-frequency signal coming from the oxide phase) nor by GIXRD (for the overwhelming glass scattering), whereas a SPR signal can be detected by optical absorption.

4 Conclusions

We have investigated the atomic structure of Cu–Ni alloy clusters embedded in silicate glasses obtained by sequential ion implantation procedure. X-ray diffraction data, collected with the grazing incidence technique, yield a value of the lattice parameter of the $Cu_{55}Ni_{45}$ alloy. X-ray absorption data confirm this finding, evidencing also oxide phases. Simulations of the optical absorption data predict a disappearance of the SPR band for alloy clusters of more than about 50% nickel content, as experimentally observed in our samples. The experimental evidence indicates that, in the case of sequential copper + nickel implants, alloy nanoparticle formation takes place: this gives a suggestion for the refinement of the cluster formation models, with the aim of better understanding the physical and chemical processes governing the synthesis of nanometer-scale particles by ion irradiation.

This work has been partially supported by Italian MURST (Coordinated Project) and CNR.

References

1. H. Hache, D. Ricard, C. Flytzanis, J. Opt. Soc. Am. B **3**, 1647 (1986).
2. E. Cattaruzza, F. Gonella, G. Mattei, P. Mazzoldi, D. Gatteschi, C. Sangregorio, M. Falconieri, G. Salvetti, G. Battaglin, Appl. Phys. Lett. **73**, 1176 (1998).
3. K. Becker, L. Yang, R.F. Haglund Jr, R.H. Magruder III, R.A. Weeks, R.A. Zuhr, Nucl. Instrum. Meth. B **59/60**, 1304 (1991).
4. H. Hosono, H. Fukushima, Y. Abe, R.A. Weeks, R.A. Zuhr, J. Non-Cryst. Solids **143**, 157 (1992).

5. L.C. Nistor, J. van Landuyt, J.D. Barton, D.E. Hole, N.D. Skelland, P.D. Townsend, J. Non-Cryst. Solids **162**, 217 (1993).
6. K. Fukumi, A. Chayahara, K. Kadono, T. Sakaguchi, Y. Horino, M. Miya, K. Fujii, J. Hayakawa, M. Satou, J. Appl. Phys. **75**, 3075 (1994).
7. R.F. Haglund Jr, L. Yang, R.H. Magruder III, C.W. White, R.A. Zuhr, Lena Yang, R. Dorsinville, R.R. Alfano, Nucl. Instrum. Meth. B **91**, 493 (1994).
8. P. Mazzoldi, F. Caccavale, E. Cattaruzza, P. Chakraborty, L. Tramontin, A. Boscolo-Boscoletto, R. Bertoncello, F. Trivillin, G. Battaglin, G.W. Arnold, Nucl. Instrum. Meth. B **91**, 505 (1994).
9. M. Falconieri, G. Salvetti, E. Cattaruzza, F. Gonella, G. Mattei, P. Mazzoldi, M. Piovesan, G. Battaglin, R. Polloni, Appl. Phys. Lett. **73**, 288 (1998).
10. M. Antonello, G.W. Arnold, G. Battaglin, R. Bertoncello, E. Cattaruzza, P. Colombo, G. Mattei, P. Mazzoldi, F. Trivillin, J. Mater. Chem. **8**, 457 (1998).
11. P. Mazzoldi, G.W. Arnold, G. Battaglin, F. Gonella, R.F. Haglund Jr, J. Nonlin. Opt. Phys. Mater. **5**, 285 (1996).
12. F. Gonella, G. Mattei, P. Mazzoldi, C. Sada, G. Battaglin, E. Cattaruzza, Appl. Phys. Lett. **75**, 55 (1999).
13. E. Cattaruzza, G. Battaglin, R. Polloni, T. Cesca, F. Gonella, G. Mattei, C. Maurizio, P. Mazzoldi, F. D'Acapito, F. Zontone, R. Bertoncello, Nucl. Instrum. Meth. B **148**, 1007 (1999).
14. P. Mazzoldi, F. Caccavale, E. Cattaruzza, A. Boscolo-Boscoletto, R. Bertoncello, A. Glisenti, G. Battaglin, C. Gerardi, Nucl. Instrum. Meth. B **65**, 367 (1992).
15. H. Hosono, Jpn J. Appl. Phys. **32**, 3892 (1993).
16. G. Battaglin, Nucl. Instrum. Meth. B **116** (1996) 102.
17. E. Cattaruzza, *5th International Conference on Advanced Materials (IUMRS-ICAM'99)*, June 13–18, 1999, Beijing (China), Nucl. Instrum. Meth. B (in press), and references therein.
18. R.H. Magruder III, D.H. Osborne, R.A. Zuhr, J. Non-Cryst. Solids **176**, 299 (1994).
19. T.S. Anderson, R.H. Magruder III, R.A. Zuhr, J.E. Wittig, J. Electron. Mater. **25**, 27 (1996).
20. R.H. Magruder III, T.S. Anderson, R.A. Zuhr, D.K. Thomas, Nucl. Instrum. Meth. B **108**, 305 (1996).
21. T.S. Anderson, R.H. Magruder III, D.L. Kinser, R.A. Zuhr, D.K. Thomas, Nucl. Instrum. Meth. B **124**, 40 (1997).
22. R. Bertoncello, F. Trivillin, E. Cattaruzza, P. Mazzoldi, G.W. Arnold, G. Battaglin, M. Catalano, J. Appl. Phys. **77**, 1294 (1995).
23. R. Bertoncello, S. Gross, F. Trivillin, F. Caccavale, E. Cattaruzza, G. Mattei, P. Mazzoldi, G. Battaglin, S. Daolio, J. Mater. Res. **14**, 2449 (1999).
24. F. Lihl, H. Ebel, W. Baumgartner, Z. Metallkunde **62**, 42 (1971).
25. R. Hultgren, P.D. Desai, D.T. Hawkins, M. Gleiser, K.K. Kelley, *Selected Values of the Thermodynamic Properties of Binary Alloys* (American Society for Metals, Ohio, 1973).
26. E. Cattaruzza, F. D'Acapito, F. Gonella, A. Longo, A. Martorana, G. Mattei, C. Maurizio, D. Thiaudière, J. Appl. Cryst. (in press).
27. M. Strobel, K.-H. Heinig, W. Möller, Nucl. Instrum. Meth. B **148**, 104 (1999).
28. G. Chen, J. Heat Transfer **118**, 539 (1999).
29. J.P. Biersack, L. Haggmark, Nucl. Instrum. Meth. **174**, 257 (1980).
30. S. Pascarelli, F. Boscherini, F. D'Acapito, J. Hrdy, C. Meneghini, S. Mobilio, J. Synchr. Rad. **3**, 147 (1996).
31. F. D'Acapito, F. Zontone, J. Appl. Cryst. **32**, 234 (1999).
32. A.P. Hammersley, S.O. Svensson, M. Hanfland, A.N. Fitch, D. Häusermann, High Pressure Res. **14**, 235 (1996).
33. U. Kreibig, M. Vollmer, *Optical Properties of Metal Clusters*, Springer Series in Materials Science (Springer, Berlin, 1995), Vol. 25.
34. J.A. Creighton, D.G. Eadon, J. Chem. Soc. Faraday Trans. **87**, 3881 (1991).
35. P.A. Lee, P.H. Citrin, P. Eisenberger, B.M. Kincaid, Rev. Mod. Phys. **53**, 769 (1981).
36. R.N.G. Wychoff, *Crystal Structure* (Wiley and Sons, New York, 1964).
37. K. Fukumi, A. Chayahara, K. Kadono, H. Kageyama, T. Akai, N. Kitamura, M. Makihara, K. Fujii, J. Hayakawa, J. Non-Cryst. Solids **238**, 143 (1998).
38. F. D'Acapito, S. Mobilio, J.R. Regnard, E. Cattaruzza, F. Gonella, P. Mazzoldi, J. Non-Cryst. Solids **232–234**, 364 (1998).
39. F. D'Acapito, S. Colonna, S. Mobilio, F. Gonella, E. Cattaruzza, P. Mazzoldi, Appl. Phys. Lett. **71**, 2611 (1997).
40. F. Gonella, F. Caccavale, L.D. Bogomolova, F. D'Acapito, A. Quaranta, J. Appl. Phys. **83**, 1200 (1998).
41. G. Licheri, G. Pinna, in *EXAFS and Near Edge Structures*, Springer Series in Chemical Physics (Springer, Berlin, 1983), Vol. 27, p. 240.
42. F. Zontone, F. D'Acapito, F. Gonella, Nucl. Instrum. Meth. B **147**, 416 (1999).
43. A.C. Larson, R.B. Von Dreele, GSAS - General Structure Analysis System, Los Alamos National Laboratory, LAUR 86 (1985).
44. P.A. Montano, G.K. Shenoy, E.E. Alp, W. Schultze, J. Urban, Phys. Rev. Lett. **56**, 2076 (1986).
45. F. D'Acapito, E. Cattaruzza, F. Gonella, S. Mobilio, J.R. Regnard, F. Spizzo, J. Phys. IV France **7**, C2-1107 (1997).
46. G. D'Agostino, Mat. Sci. Forum **195**, 149 (1995).
47. P.B. Johnson, R.W. Christy, Phys. Rev. B **6**, 4370 (1972).
48. Landolt-Börnstein, *Eigenschaften der materie in ihren aggregatzuständen, 8.teil - Optische konstanten* (Springer Verlag, Berlin, 1962).
49. D.W. Lynch, W.R. Hunter, in *Handbook of Optical Constant of Solids*, edited by E.D. Palik (Academic Press, San Diego, 1998).
50. W.C. Huang, J.T. Lue, Phys. Rev. B **49**, 17279 (1994).
51. S. Åsbrink, L.J. Norrby, Acta Cryst. B **26**, 8 (1970).
52. H.G. Fritsche, R.E. Benfield, Z. Phys. D **26**, S15 (1993).
53. J.A. Duffy, F.G.K. Baucke, J. Phys. Chem. **99**, 9189 (1995).